



# A high-performance waterborne polymeric composite coating with long-term anti-corrosive property based on phosphorylation of chitosan-functionalized $Ti_3C_2T_x$ MXene

Xiaoling He<sup>1</sup> · Sihao Li<sup>1</sup> · Rongbiao Shen<sup>1</sup> · Yanqi Ma<sup>1</sup> · Li Zhang<sup>1</sup> · Xinxin Sheng<sup>1,2,3</sup> · Ying Chen<sup>1</sup> · Delong Xie<sup>2</sup> · Jintao Huang<sup>1,4</sup>

Received: 5 October 2021 / Revised: 18 November 2021 / Accepted: 30 November 2021 / Published online: 11 January 2022  
© The Author(s), under exclusive licence to Springer Nature Switzerland AG 2021

## Abstract

As a newly discovered two-dimensional (2D) material, MXene has attracted much attention because of its fascinating physicochemical properties. However, the issue of agglomeration has limited its application in anti-corrosive polymeric coatings. Herein, a novel nanofiller, phosphoric acid-modified chitosan (mCS)-functionalized MXene (fMX), has been successfully constructed and used to endow waterborne epoxy (WEP) coatings with brilliant corrosive resistance. Electrochemical results demonstrate that the  $|Z_{0.01 Hz}|$  value for 0.2 wt% fMX/WEP composite coating ( $4.73 \times 10^7 \Omega \text{ cm}^2$ ) is more than two orders of magnitude higher than that of the blank WEP ( $2.09 \times 10^5 \Omega \text{ cm}^2$ ) and the corrosion current density value of 0.2 wt% fMX/WEP maintains above  $5.44 \times 10^{-9} \text{ A/cm}^2$  after soaking in 3.5 wt% NaCl solution for 50 days. It is nearly two orders lower than that of blank WEP ( $5.23 \times 10^{-7} \text{ A/cm}^2$ ). Thus, this novel mCS-functionalized MXene can serve as an effective composite nanofiller for preparing MXene-based high-performance anti-corrosive coatings.

**Keywords**  $Ti_3C_2T_x$  MXene · Phosphorylated chitosan · Waterborne epoxy coating · Corrosive resistant

## 1 Introduction

Metal corrosion has caused great damage to society and industry, since it severely impairs the performance and service life of metal materials through accelerating their

invalidation in the process of service [1–3]. Several strategies have been developed to slow down or avoid metal corrosion, such as surface modification, cathodic protection, anodic protection, and protective coatings. Applying an organic coating on the metal surface can prevent the metal substrate from contacting corrosive media ( $H_2O$ ,  $O_2$ ,  $Cl^-$ , etc.), which is one of the most effective anti-corrosive method [4]. Among various organic coatings, epoxy coatings are extensively employed in the anti-corrosive field due to their excellent performances, such as superior adhesion, high crosslinking density, excellent chemical resistance, and low shrinkage [5–7]. Due to the increasing environmental awareness and restrictions on volatile organic compounds in many countries, waterborne epoxy coatings (WEP) have captured substantial attention [8]. However, due to the high crosslinking density of epoxy network and the evaporation of water during curing process of the coating, micro-pores and micro-crack are easily generated in the coating, causing corrosive medium to reach the substrate/coating interface [9]. Fortunately, doping 2D nanomaterials or adding corrosion inhibitors are effective strategies to improve corrosion resistance of epoxy coatings.

Recently, 2D nanomaterials, including graphene [10], graphene oxide (GO) [11], boron nitride [12], etc., have

✉ Xinxin Sheng  
xinxin.sheng@gdut.edu.cn; cexxsheng@gmail.com

✉ Ying Chen  
chenying@gdut.edu.cn

<sup>1</sup> Guangdong Provincial Key Laboratory of Functional Soft Condensed Matter, School of Materials and Energy, Guangdong University of Technology, Guangzhou 510006, China

<sup>2</sup> Yunnan Provincial Key Laboratory of Energy Saving in Phosphorus Chemical Engineering and New Phosphorus Materials, The Higher Educational Key Laboratory for Phosphorus Chemical Engineering of Yunnan Province, Kunming 650500, China

<sup>3</sup> Guangdong Provincial Key Lab of Green Chemical Product Technology, South China University of Technology, Guangzhou 510640, China

<sup>4</sup> Key Laboratory of Polymer Processing Engineering, Ministry of Education, South China University of Technology, Guangzhou 510640, China

attracted increasing attention in the field of anti-corrosive [13]. MXene is a newly discovered 2D nanomaterial. Its typical formula is  $M_{n+1}X_nT_x$ , where M stands for the early transition metal;  $n = 1, 2, \text{ or } 3$ ; X is C and/or N elements; and  $T_x$  stands for MXene's surface-terminating groups (O,  $-OH$ , or  $-F$ ) [14]. MXene is synthesized by etching A (a group IIIA or IVA element) layer from  $M_{n+1}AX_n$  phase [15]. The excellent mechanical property and large specific surface area of  $Ti_3C_2T_x$  is expected to enhance the barrier and anti-corrosive performance of epoxy resin [16]. However, like many other 2D nanomaterials, performance is affected by the strong tendency of interlayer aggregation, due to van der Waals forces and hydrogen bonding [17]. Thus, in order to broaden the application fields of MXene, it is essential to improve the dispersibility of MXene as functional fillers in the polymeric coatings. To overcome this challenge, Yan et al. [18] synthesized amino-functionalized  $Ti_3C_2T_x$  (f-M) and showed that the dispersibility and compatibility of f-M in the coatings have been greatly improved. The results indicated that the coating containing 0.5 wt% f-M nanosheets exhibited the best anti-corrosive property. Similar to graphene, due to the formation of electrode by the highly conductive network of MXene in the coating matrix, it may cause opposite protective effect [19, 20]. Cai et al. [21] synthesized a  $Ti_3C_2T_x$  MXene/polyaniline nanohybrid via in situ redox polymerization of aniline in MXene dispersion, confirming that the nanohybrid-containing coating exhibited the best anti-corrosive performance. Therefore, it is necessary to find a method that cannot only ameliorate the dispersibility of MXene in polymeric coatings, but also inhibit galvanic corrosion.

Chitosan (CS), a N-acetylated derivative of chitin, is the second most abundant natural polysaccharide on the globe. CS has been employed in many domains owing to its exceptional performances such as biocompatible, non-toxic, anti-bacterial, and biodegradability. Furthermore, CS and its derivatives were also used as an eco-friendly and effective corrosion inhibitor because of the presence of  $-NH_2$  and  $-OH$  [22, 23]. Fayyad et al. [24] synthesized oleic acid-modified CS/GO and coated it on carbon steel. The results suggested that the corrosion resistance of oleic acid-modified CS/GO film was 100 times higher than that of blank chitosan coating. Ruhi et al. [25] added the CS-polyppyrrrole- $SiO_2$  composites to epoxy resin and coated it on steel. Tafel plots showed that the epoxy coating loaded with 2.0 wt% composite had higher corrosion protection efficiency (99.99%). Abd El-Fattah et al. [26] reported that the CS-epoxy composite coating had lower corrosion rates than that of pure coating. Nevertheless, poor solubility properties of CS in aqueous solutions have severely limited its application. Previous studies have shown that the introduction of phosphoric acid onto chitosan could effectively improve the

chelating property and solubility property [27]. Nevertheless, no investigation can be discovered in the open literature on the application of mCS to functionalize MXene for anti-corrosive WEP coatings.

Hence, in this work, the phosphorylated chitosan-functionalized MXene nanocomposites were synthesized, which not only improved the dispersion state and compatibility of MXene with the polymer matrix, but also inhibited galvanic corrosion and enhanced the adhesion between the coating and the substrate. Afterwards, the chemical and physical structure, thermal stability, and morphologies of mCS, MXene, and fMX were analyzed through FTIR, XPS, XRD, TGA, FESEM, and TEM. Furthermore, the cross-section of the coating was detected via SEM-EDS mapping, and the anti-corrosive property of as-prepared WEP composite coatings was evaluated by electrochemical impedance spectroscopy (EIS) and polarization curve. This work provides a promising strategy for the fabrication of novel MXene-based nanofillers in the long-term anti-corrosive polymeric coating fields.

## 2 Experimental section

First, CS was modified by phosphoric acid at 120 °C, resulting the mCS. Next, MXene, 2D nanosheet material, were obtained via in situ hydrofluoric acid and  $Li^+$  ions intercalation. Hereafter, MXene nanosheets were modified by mCS to get mCS-functionalized MXene (fMX). Finally, WEP paints with 0.2 wt% fMX were prepared. The experimental process is exhibited in Fig. 1. More specific experimental operations and characterizations are recorded in the supporting information.

## 3 Results and discussion

### 3.1 Chemical and physical properties of MXene, mCS, and fMX

#### 3.1.1 FTIR analysis

The functional groups of CS, mCS, MXene, and fMX were depicted by FTIR. Figure 2a shows the characteristic peak at  $1593\text{ cm}^{-1}$ , which is from the N-H deformation of amino group. Furthermore, the absorption peaks at 3423, 1421, 1157, and  $1031\text{ cm}^{-1}$  are assigned to the  $-OH$  stretching, C-N stretching of  $C-NH_2$ , C-O-C stretching of asymmetric bridge oxygen, and C-O stretching of  $-CH_2-OH$ , respectively [28]. For mCS, the new peaks at 1283 and  $1093\text{ cm}^{-1}$  represent P=O stretching and P-O stretching from phosphate. Moreover, the N-H deformation peak of  $NH_2$  at  $1593\text{ cm}^{-1}$  almost disappears, demonstrating that the amino

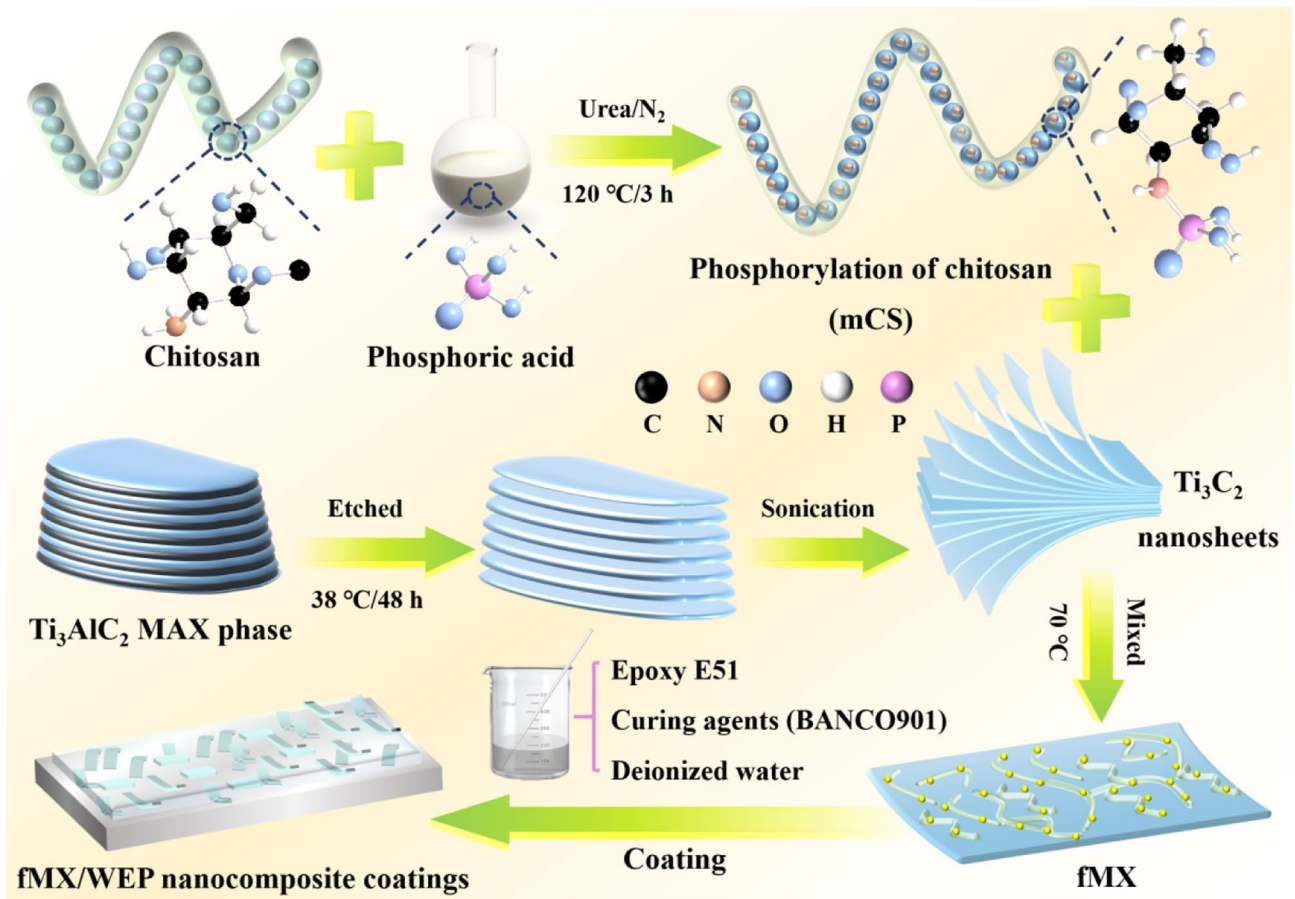


Fig. 1 The schematic graph of the preparation process of mCS, MXene, fMX, and fMX/WEP nanocomposite coatings

group of the CS reacts with phosphoric acid. Obviously, the characteristic peak at  $1406\text{ cm}^{-1}$  is derived from the red shift of C–N stretching of C–NH<sub>2</sub> at  $1421\text{ cm}^{-1}$ , suggesting

forming chemical bonds between phosphate groups and amino [29]. In short, the phosphate groups are successfully grafted onto the CS by forming N–P bonds.

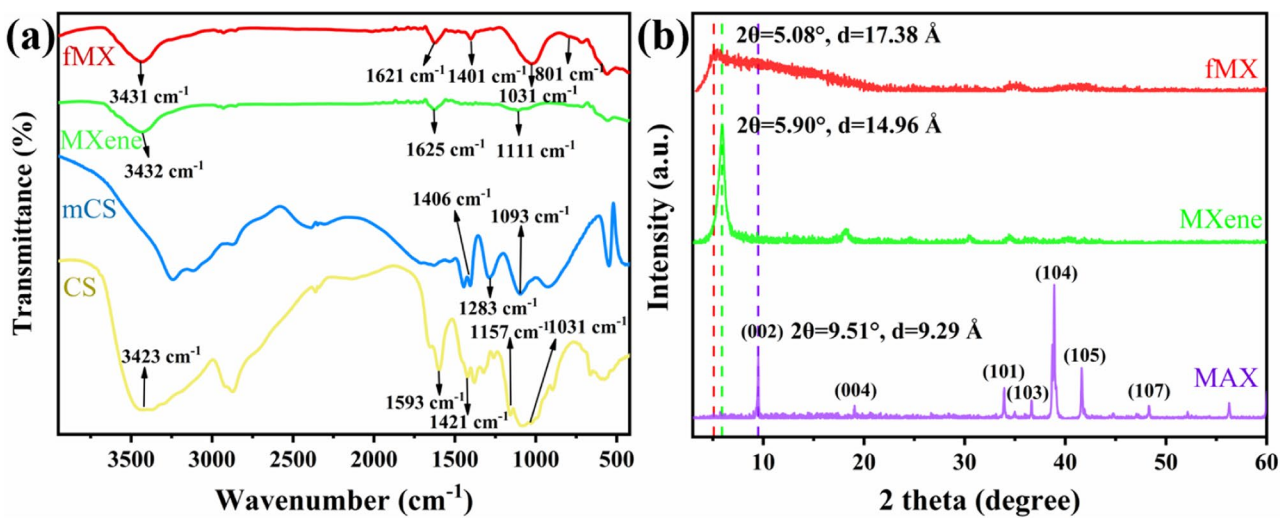


Fig. 2 a The FTIR spectra of CS, mCS, MXene, and fMX; b The XRD curves of MAX phase, MXene, and fMX

For MXene, the absorption peaks of  $-\text{OH}$  occur at  $3432$  and  $1625\text{ cm}^{-1}$ , and the vibration peaks of  $-\text{C}-\text{O}$  occur at  $1111\text{ cm}^{-1}$  [30]. After modification by mCS,  $-\text{OH}$  peaks of fMX are diverted to  $3431$  and  $1621\text{ cm}^{-1}$ , respectively. The red shift of  $-\text{OH}$  peak may be because of electron-donating group of mCS, intramolecular and/or intermolecular hydrogen bonding. It should be noted that the  $\text{P}=\text{O}$  stretching of mCS almost completely disappears and a faint  $\text{Ti}-\text{O}-\text{P}$  peak at  $801\text{ cm}^{-1}$  appears, due to the hydroxyl groups on the surface of MXene react with mCS to form  $\text{Ti}-\text{O}-\text{P}$  bonds [31].

### 3.1.2 XRD

To further investigate the crystal structure composition of MAX, MXene, and fMX, XRD characterization was conducted, as shown in Fig. 2b. Peaks of MAX phase at  $2\theta=9.51^\circ$ ,  $38.83^\circ$ ,  $41.60^\circ$ , and  $48.32^\circ$  correspond to (002), (104), (105), and (107) peaks, respectively [32]. After etching by wet chemical method, the peaks of MAX phase at  $2\theta=33.98^\circ$ ,  $36.65^\circ$ ,  $38.83^\circ$ ,  $41.60^\circ$ , and  $48.32^\circ$  almost disappear. Moreover, the (002) peak of MXene shifts from  $9.51$  to  $5.90^\circ$ , suggesting that the  $d$ -spacing of MXene increased from  $9.29$  to  $14.96\text{ \AA}$ . In brief, these consequences indicate that the Al layers were smoothly etched from the MAX phase and MXene is successfully synthesized [33]. After

function by mCS, the XRD curve of fMX illustrates a wide peak at about  $5.08^\circ$ , implying that the  $d$ -spacing of MXene is further increased ( $17.38\text{ \AA}$ ). This may be caused by the intercalation of mCS, or the chemical modification of MXene, thus enlarging the inter-layer distance [34, 35]. Meanwhile, the broadening of the (002) peak is probably due to crystal lattice defects caused by the modification process [36].

### 3.1.3 XPS analysis

The chemical composition of the as-obtained samples was further ascertained by XPS. In Fig. 3b, the deconvoluted N 1s XPS spectrum of CS is shown; the two subpeaks separated correspond to  $\text{N}-\text{H}$  ( $399.8\text{ eV}$ ) and  $\text{N}-\text{C}=\text{O}$  ( $401.8\text{ eV}$ ) bonds, respectively [37, 38]. For mCS, it is easily observed the signal peak of  $\text{N}-\text{P}$  at  $401.8\text{ eV}$ , meaning that phosphate groups have been successfully attached to the amino group of CS. To verify the above conclusion further, the thermal stability of CS and mCS has been researched by TGA. In Fig. S1, the first stage of weight loss at  $25\text{--}100^\circ\text{C}$  is owing to the loss of adsorbed and bound water. However, the second stage of weight loss for CS and mCS is approximately  $210^\circ\text{C}$  and  $170^\circ\text{C}$ , respectively. This may be due to introduction of phosphate groups, thereby reducing the amount of hydrogen bonds [39].

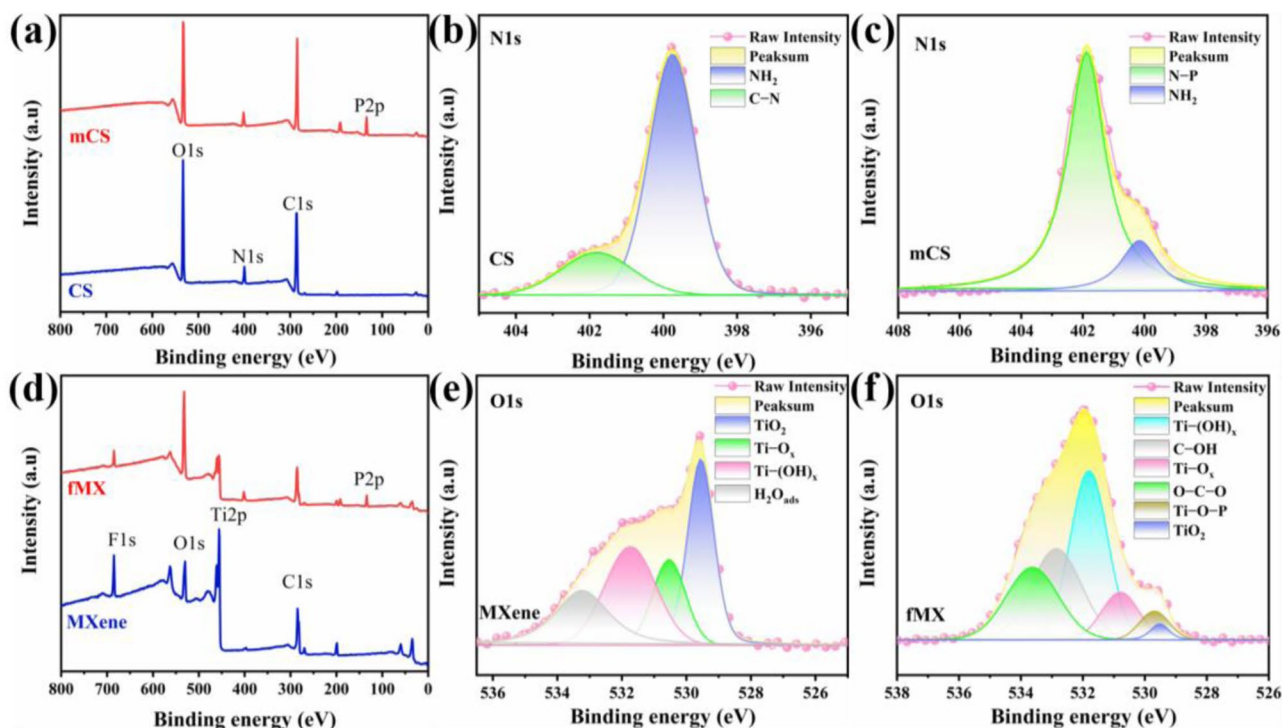


**Fig. 3** a XPS spectra of pristine CS and mCS; b N 1s spectra of CS; c N 1s spectra of mCS; d XPS spectra of pristine MXene and fMX; e O 1s spectra of MXene; f O 1s spectra of fMX

For MXene, the O 1 s XPS spectrum (Fig. 3e) presents four peaks, corresponding to  $\text{TiO}_2$  (529.5 eV),  $\text{Ti-O}_x$  (530.6 eV), and  $\text{Ti-(OH)}_x$  (531.7 eV) and absorbing water (533.2 eV), respectively [40]. Compared with MXene, three new peaks in the XPS spectrum of fMX appear at 532.8, 533.6, and 529.7 eV, which represent C–OH bond, O–C–O bond, and Ti–O–P bond, respectively. This can be attributed to the successful grafting of mCS onto MXene [41]. Combining the results of FTIR and XPS, it can be found that mCS has been successfully grafted onto MXene, which may bring benefits to the compatibility of MXene and epoxy coatings.

### 3.2 Morphology of MAX, MXene, and fMX nanocomposites

The surface morphology of the synthesized materials was compared and qualified by FESEM and TEM. As shown in Fig. 4a, b, d, the MAX phase has a transition from the block-like to the accordion-like by a wet chemical etching method, and then a 2D MXene material is obtained by physical stripping [42]. From Fig. 4b, c, the synthesized MXene is a very thin and clean layer nanosheet. After modification with mCS, the high-resolution TEM image of fMX shows that there are patches and shadows on the MXene surface (Fig. 4e) [43]. Based on the above discussion, MXene may have a chemical reaction with mCS chains or oxidized during the modification process [44].

### 3.3 Characterization of WEP coatings

The fracture surfaces of blank WEP, MXene/WEP, 0.2 wt% fMX/WEP, and 0.5 wt% fMX/WEP were fractured in liquid nitrogen. For blank WEP coating (Fig. 5a, e), the appearance is sleek but with evident micro-pores, which is the result of the incomplete coalescence of epoxy emulsion droplets and fast water evaporation during the film formation process. With the introduction of MXene nanosheets, the fracture surface is extremely uneven (Fig. 5b, f), with many bumps and holes. This is due to the poor compatibility of MXene with polymer, leading to emergence of defects [45]. While as for 0.2 wt% fMX/WEP coating (Fig. 5c, g), it can be seen that the texture of the fractured surface is quite uniform and rougher. The fMX nanosheets cover the micro-pores of coating, suggesting that after being medicated by mCS, fMX has better interfacial adhesion and compatibility with coating matrix, thereby prolonging the torturous diffusion pathways for the permeation of corrosive mediums. As we all know, the reduction of porosity and homogenous distribution of fMX are conducive to the improvement of anti-corrosive performance [46]. However, in the case of 0.5 wt% fMX/WEP coating (Fig. 5d, h), obvious nodes and bumps are observed, which may be due to agglomeration of fMX in high amount in the coating [47].

The EDS mappings of the cross-section of 0.2 wt% fMX/WEP coating are used to evaluate the distribution of nano-filler in coating. It is known that C, N, and O elements exist in both blank epoxy coating and mCS, Ti element is the characteristic of MXene, and P element is the characteristic

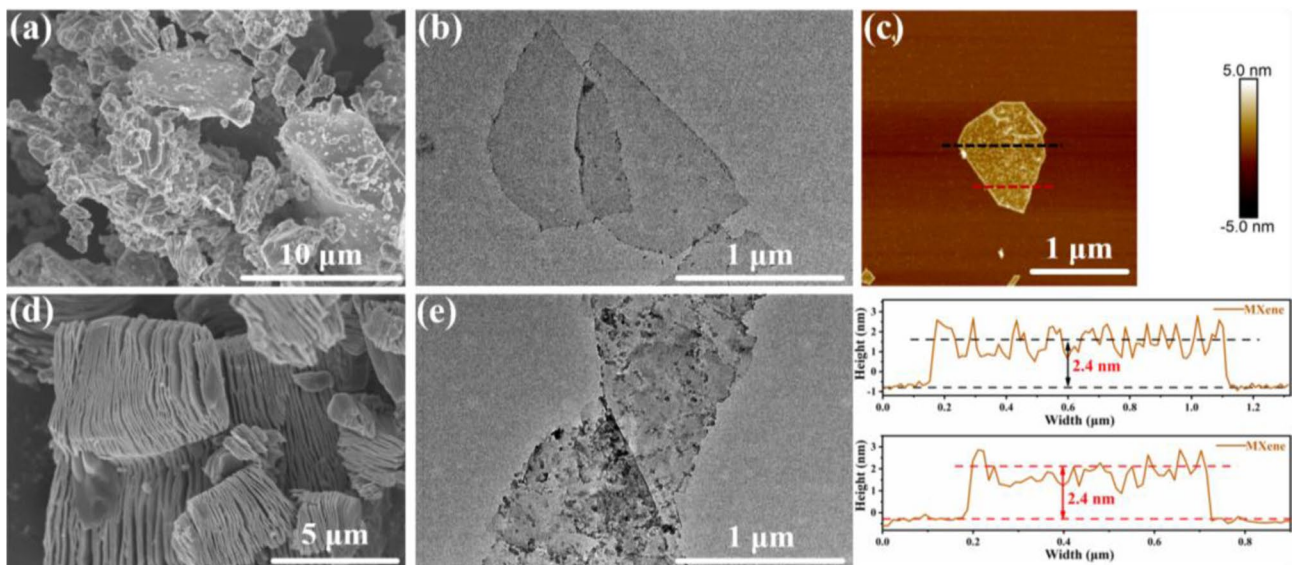


**Fig. 4** FESEM images of **a** MAX phase and **d** accordion-like MXene; the AFM image of **c** MXene nanosheets; the TEM image of **b** MXene nanosheets and **e** fMX nanosheets

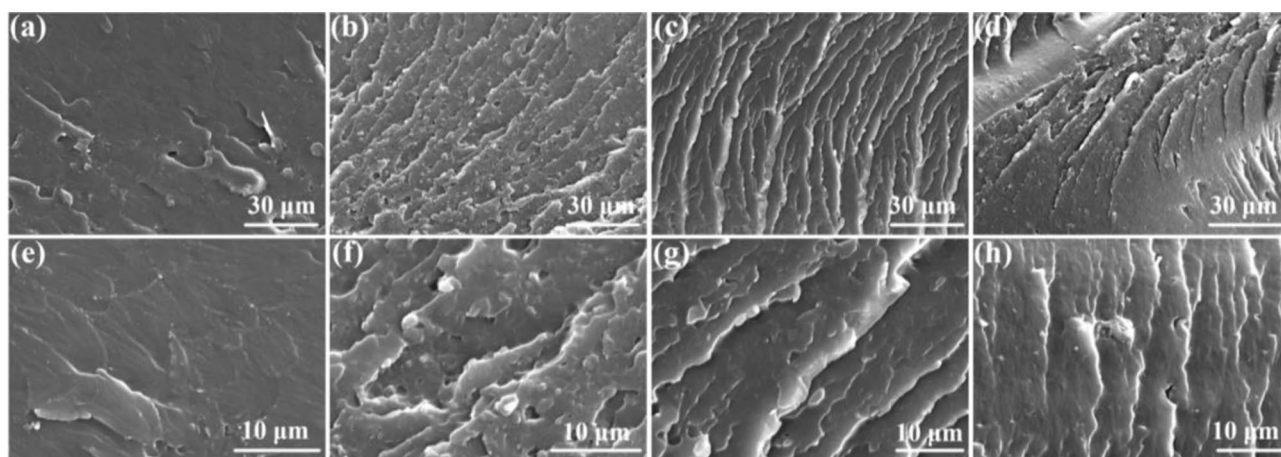


**Fig. 5** SEM images of fracture surface of (a, e) blank WEP, (b, f) 0.2 wt% MXene/WEP, (c, g) 0.2 wt% fMX/WEP, and (d, h) 0.5 wt% fMX/WEP coating

of mCS. The distribution of Ti and P elements in the polymer coating is uniform as described for Fig. 6e, f, which points that fMX is very uniformly dispersed in the WEP coating and this fact may be helpful to advance of anti-corrosive capability [48]. DSC was carried out to research the effect of different 2D nanofillers on the degree of crosslinking of coatings. In Fig. S2, the  $T_g$  value of the coatings have increased in varying degrees after doping with nanomaterials. It is considered that the epoxy groups of WEP can react with ostensible active groups of MXene, thus increasing the crosslinking density of the coating [49].

### 3.4 Corrosion protection property measurement

The long-term anti-corrosive ability of fMX after being incorporated in WEP coating is examined by EIS in NaCl solution (3.5 wt%) for up to 50 days. The results were fitted by equivalent electric circuits (EECs) and plotted as EIS plots, as shown in Fig. 7 [50]. Figure 7a–c depict the Nyquist image of different coatings after immersion for 1th, 10th, and 50th day, respectively. Firstly, as the immersion time increases, the diameter at high frequency decreases for all coatings. However, results show that the epoxy composite

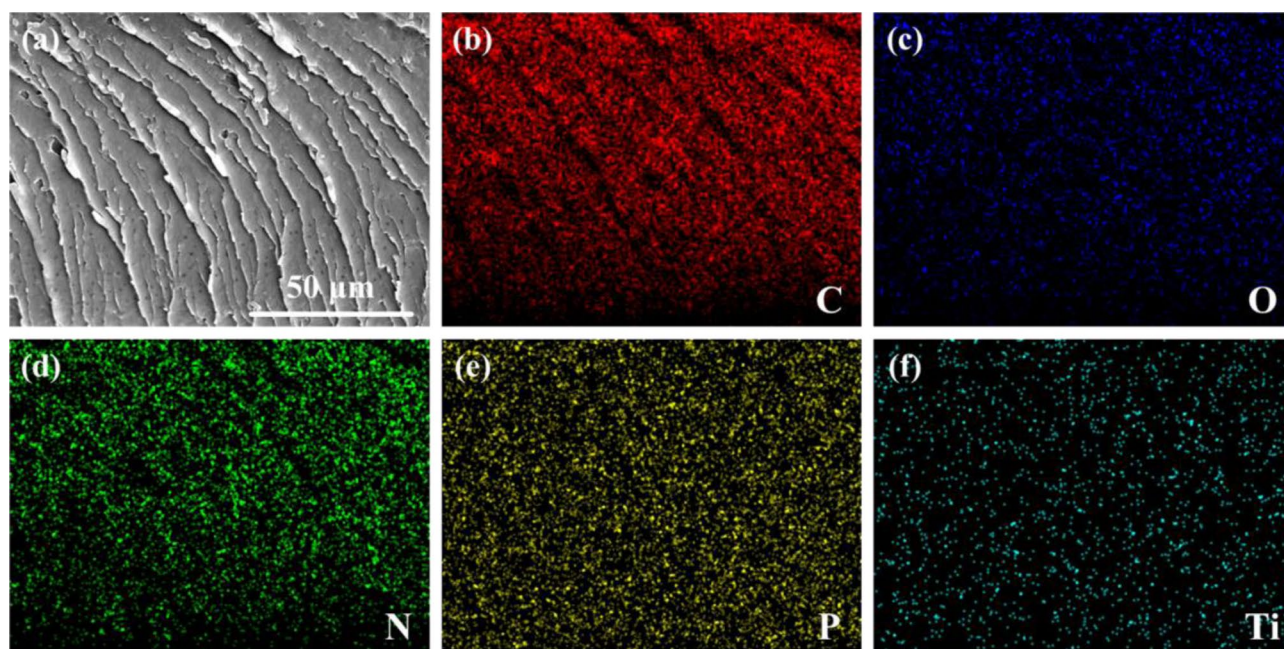


**Fig. 6** The SEM image of 0.2 wt% fMX/WEP coating (a) and its EDS mapping of C element (b), O element (c), N element (d), P element (e), and Ti element (f)

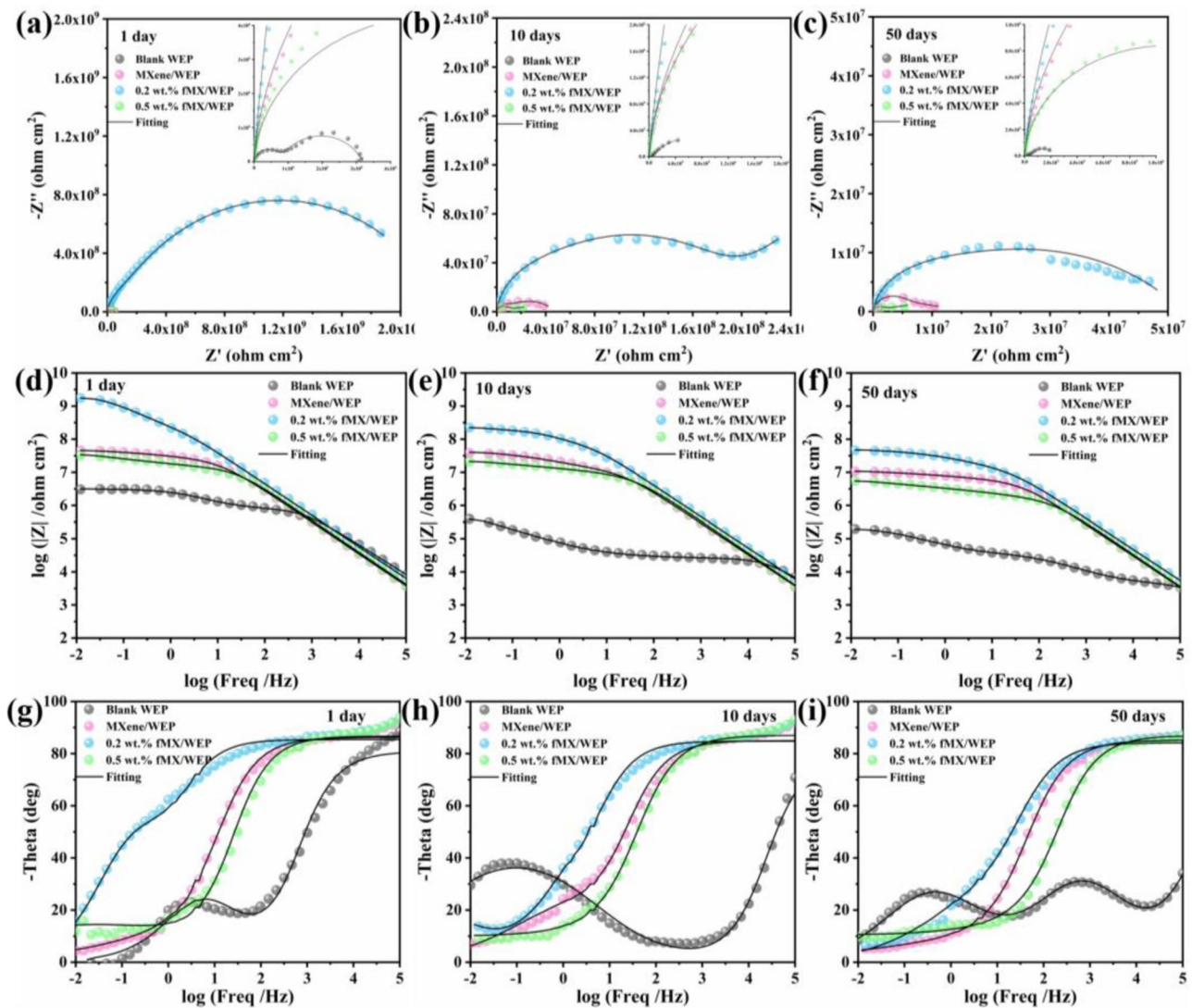


**Fig. 7** Nyquist (**a, b, c**), Bode (**d, e, f**), and phase (**g, h, i**) plots of blank WEP, 0.2 wt% MXene/WEP, 0.2 wt% fMX/WEP, and 0.5 wt% fMX/WEP coatings after 1, 10, and 50 days immersed in the 3.5 wt% NaCl aqueous solution

containing 0.2 wt% fMX shows the maximum diameter at high frequency, compared with other coatings, after 50 days of immersion. It is clearly depicting that the incorporation of fMX in the polymer remarkably increases the barrier property of the polymer. Besides, in the bode plots, the lowest-frequency modulus of the four coatings has conspicuous distinction (Fig. 7d–f). And, after 50 days of immersion, the lowest-frequency modulus of 0.2 wt% fMX/WEP coating ( $4.73 \times 10^7 \Omega \text{ cm}^2$ ) is much higher than that of blank WEP coating ( $2.09 \times 10^5 \Omega \text{ cm}^2$ ).

In addition, in Fig. 7g–i, the data of high-frequency region (i.e.,  $10^3$ – $10^5$  Hz) frequently means barrier performance of WEP coatings, and the data of middle-to-low-frequency region (i.e.,  $10^{-2}$ – $10^3$  Hz) frequently means the generation of the corrosion reaction [51]. The blank WEP

coating has changed from two-time constant to three-time constant after 50 days of immersion, which is not uncommon and may be due to the long immersion time and uncontrollable charge transfer reaction of the corrosive medium to reach the coating substrate, resulting in degradation of the coating [52, 53]. Moreover, all coatings exhibit high Bode phase angle at high-frequency region and low Bode phase angle at middle-to-low-frequency region except blank coating.

To intuitively compare the corrosion behavior of the coatings, the impedance modulus corresponding to the 0.01 Hz frequencies and the breakpoint frequency corresponding to the  $45^\circ$  phase angle are plotted in Fig. 8. The  $|Z_{0.01 \text{ Hz}}|$  is positively correlated with the protective performance of coatings [48]. In Fig. 8a,  $|Z_{0.01 \text{ Hz}}|$  of the 0.2 wt% fMX/WEP coating ( $4.73 \times 10^7 \Omega \text{ cm}^2$ ) is more than two orders of magnitude

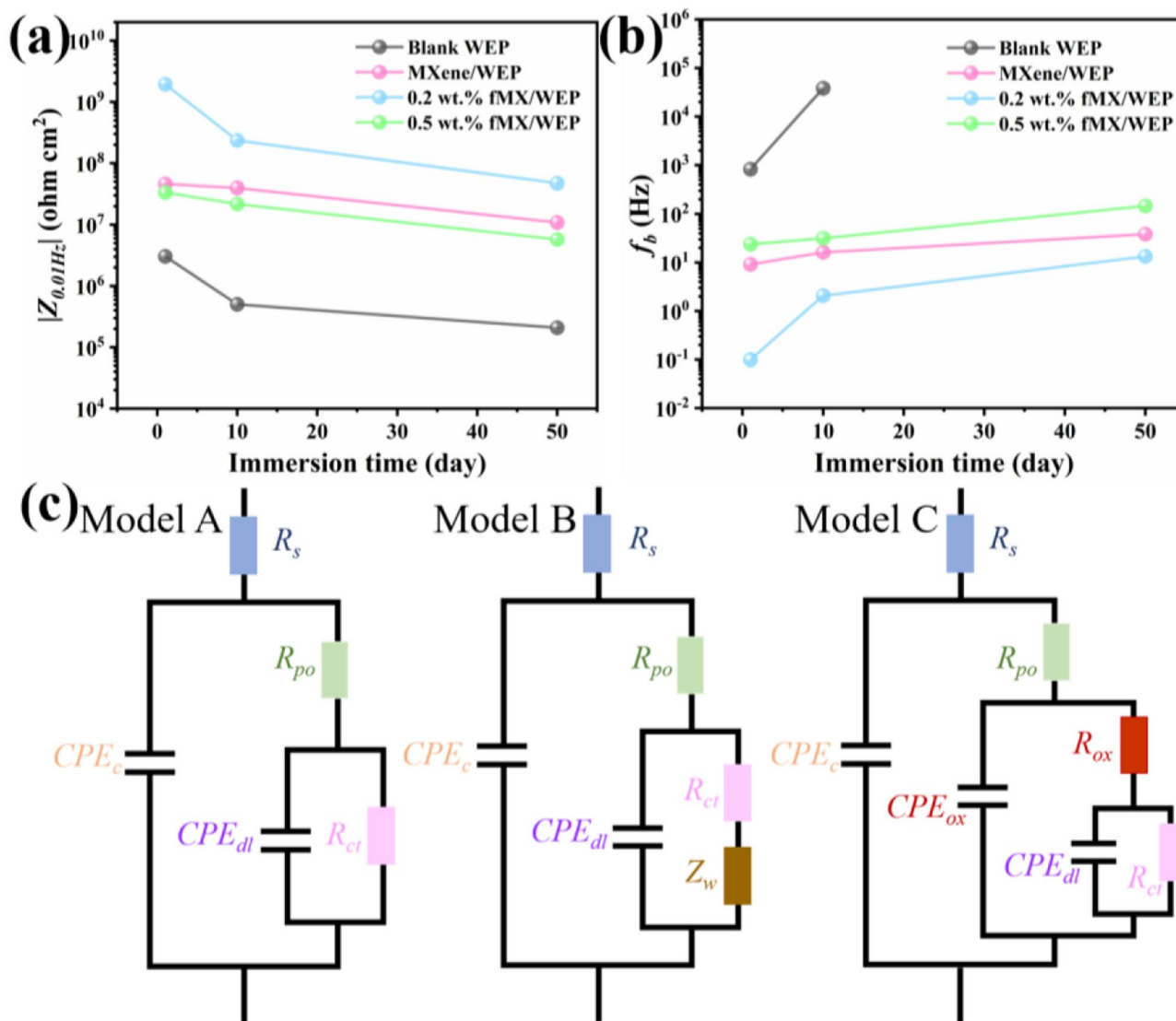


**Fig. 8** Impedance modulus at **a** 0.01 Hz frequencies ( $|Z_{0.01 \text{ Hz}}|$ ) and **b** breakpoint frequencies at  $45^\circ$  phase angle ( $f_b$ ) of blank WEP, 0.2 wt% MXene/WEP, 0.2 wt% fMX/WEP, and 0.5 wt% fMX/WEP coatings

after 1 day, 10 days, and 50 days exposure to 3.5 wt% NaCl aqueous. **c** The equivalent electrical circuits (EECs)

higher than that of blank WEP coating ( $2.09 \times 10^5 \Omega \text{ cm}^2$ ). Results confirm that MXene modification by mCS helps the fMX maintain its barrier and anti-corrosive performances in polymer, because it promotes the compatibility between the nanofillers and the coating. However, when the doping of fMX was increased from 0.2 to 0.5 wt%, the  $|Z_{0.01 \text{ Hz}}|$  of coating undergoes a grave reduction (from  $4.73 \times 10^7$  to  $5.76 \times 10^6 \Omega \text{ cm}^2$ ), which is almost one order of magnitude lower contrasted with 0.2 wt% fMX/WEP coating. The fMX nanofiller agglomeration may be caused by excessive mass fraction [54].

Furthermore, the microscopic delaminated areas of coating from metal matrix is evaluated by  $f_b$  [55]. For blank WEP coatings (Fig. 8b), the initial  $f_b$  is 825.20 Hz, and the

value of  $f_b$  increases to  $3.83 \times 10^4$  Hz after the 10 days of immersion. In addition, the blank WEP coating does not have a  $45^\circ$  phase angle after 50 days of immersion, which means that the blank WEP coating is more likely to blister or even crack. Unexpectedly, the  $f_b$  for 0.2 wt% fMX/WEP is only 0.10 Hz at 1 day, which is lower than other coatings, and it is still as low as 13.40 Hz after 50 days of immersion, indicating that the incorporation of well-dispersed fMX can prevent corrosion ions from reaching the substrate, and the adhesion between polymer and substrate cannot be destroyed. Moreover, the best results are achieved with the 0.2 wt% fMX/WEP coating, which also can be attributed to the excellent chelating effect of the grafted phosphate groups in fMX [56].



In Fig. 8c, all the EIS results are fitted by three equivalent electrical circuits (EECs), which model A is used to fit the data of two-time constants. In model A,  $R_{ct}$ ,  $R_{po}$ , and  $R_s$  symbolize charge transfer resistance, pore resistance, and solution resistance, respectively. The  $CPE_c$  and  $CPE_{dl}$  simulate the non-constant phase capacitance of the coating and non-constant phase capacitance of the double layer, respectively. In model B,  $Z_w$  represents Warburg impedance. As the soaking time increases, the coating is severely damaged, e.g., the blank coating, the model C is used to fit. The  $CPE_{ox}$  and  $R_{ox}$  are used to model oxide layer [57]. The fitting results are sorted in Table S1. To intuitively contrast the various data of coating, the main data is plotted in Fig. 9.

$R_{po}$  is related to the pore area of coating surface and interface blistering area and inversely proportional to porosity and foaming rate of coating [58]. In Fig. 9a,  $R_{po}$  of blank coating suffers a serious decrease (from  $8.10 \times 10^5$  to  $4.65 \times 10^3 \Omega \text{ cm}^2$ ), which is over two orders of magnitude lower contrasted to its initial condition. This indicates that the corrosive media continuously diffuse into the polymer matrix, leading to the deterioration of composite coating. Surprisingly, 0.2 wt% fMX/WEP coating exhibits the highest value of  $R_{po}$  ( $1.09 \times 10^7 \Omega \text{ cm}^2$ ) over 50 days. This is owing to the remarkable compatibility of fMX with WEP coating, which leads to fewer faults in coating, thus resulting in improved anti-corrosive performance of coating. In addition,  $R_{ct}$  and  $CPE_{dl}$  exhibit response of double layer at epoxy composite/steel interface [59]. Observation of  $R_{ct}$  and

$CPE_{dl}$  indicate that the incorporation of fMX could excellently improve the barrier property of composite coatings. These outcomes show that anti-corrosive capacities of polymer are dramatically increased via addition of fMX with appropriated content in WEP.

For further investigations, the composite coatings were subjected to PD test after soaking in NaCl solution for 50 days. By the Faraday's law formula, Stern-Geary equation, and Tafel extrapolation, some crucial electrochemical parameters can be obtained to assess the anti-corrosive performance of coatings, such as corrosion rate ( $CR$ ), corrosion, polarization resistance ( $R_{po}$ ), current density ( $I_{corr}$ ), and corrosion potential ( $E_{corr}$ ). The gradients of anodic and cathodic are anode ( $b_a$ ) and cathode ( $b_c$ ), respectively [45]. In general, an inferior  $I_{corr}$  implies an inferior  $CR$  and advanced anti-corrosive capacity [55]. In Table S2,  $I_{corr}$  of 0.2 wt% fMX/WEP is  $5.44 \times 10^{-9} \text{ A/cm}^2$ , which is two orders of magnitude lower than that of neat coating ( $5.23 \times 10^{-7} \text{ A/cm}^2$ ). It is demonstrated that 0.2 wt% fMX/WEP coating possesses better anti-corrosive property.

### 3.5 Characterization of corrosive products

To further explore the corrosive capability of all WEP coatings, the corrosion products of metal were analyzed. The corrosion morphology of the metal (the coating had been peeled off) was described by SEM and EDS. The O element content of coatings is in order of 0.2 wt% fMX/WEP coating (4.19

**Fig. 9** The plots of **a** coating resistance ( $R_{po}$ ), **b** charge transfer resistance ( $R_{ct}$ ), **c** coating capacitance ( $CPE_c$ ), and **d** double layer capacitance ( $CPE_{dl}$ ) of blank WEP, 0.2 wt% MXene/WEP, 0.2 wt% fMX/WEP, and 0.5 wt% fMX/WEP coatings after 1 day, 10 days, and 50 days exposure to 3.5 wt% NaCl solution

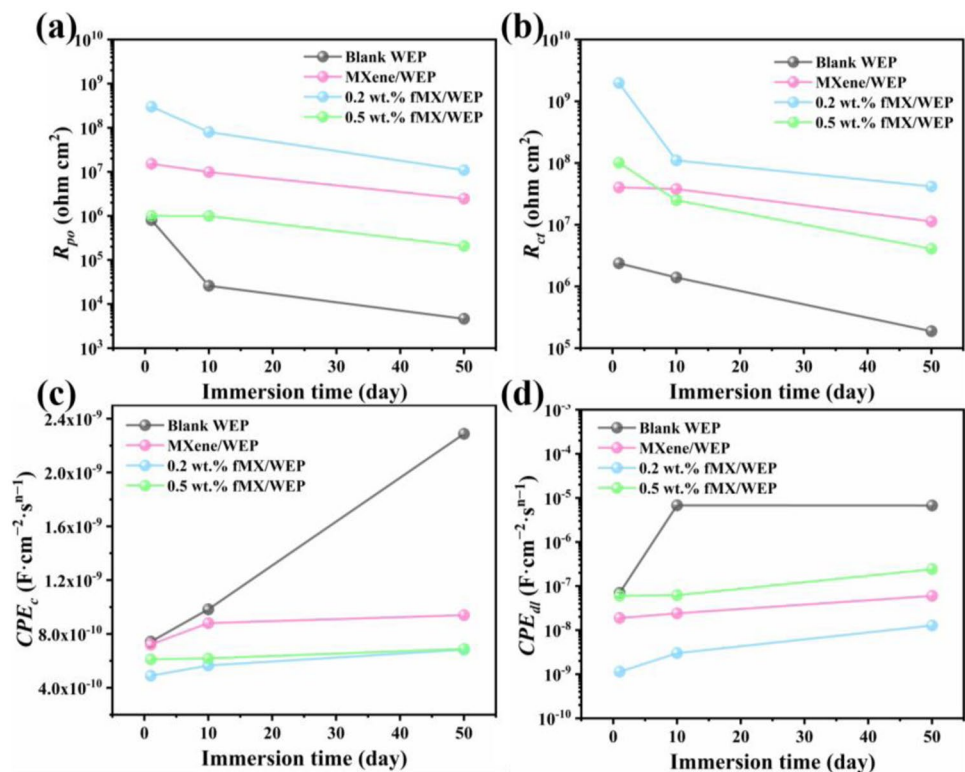
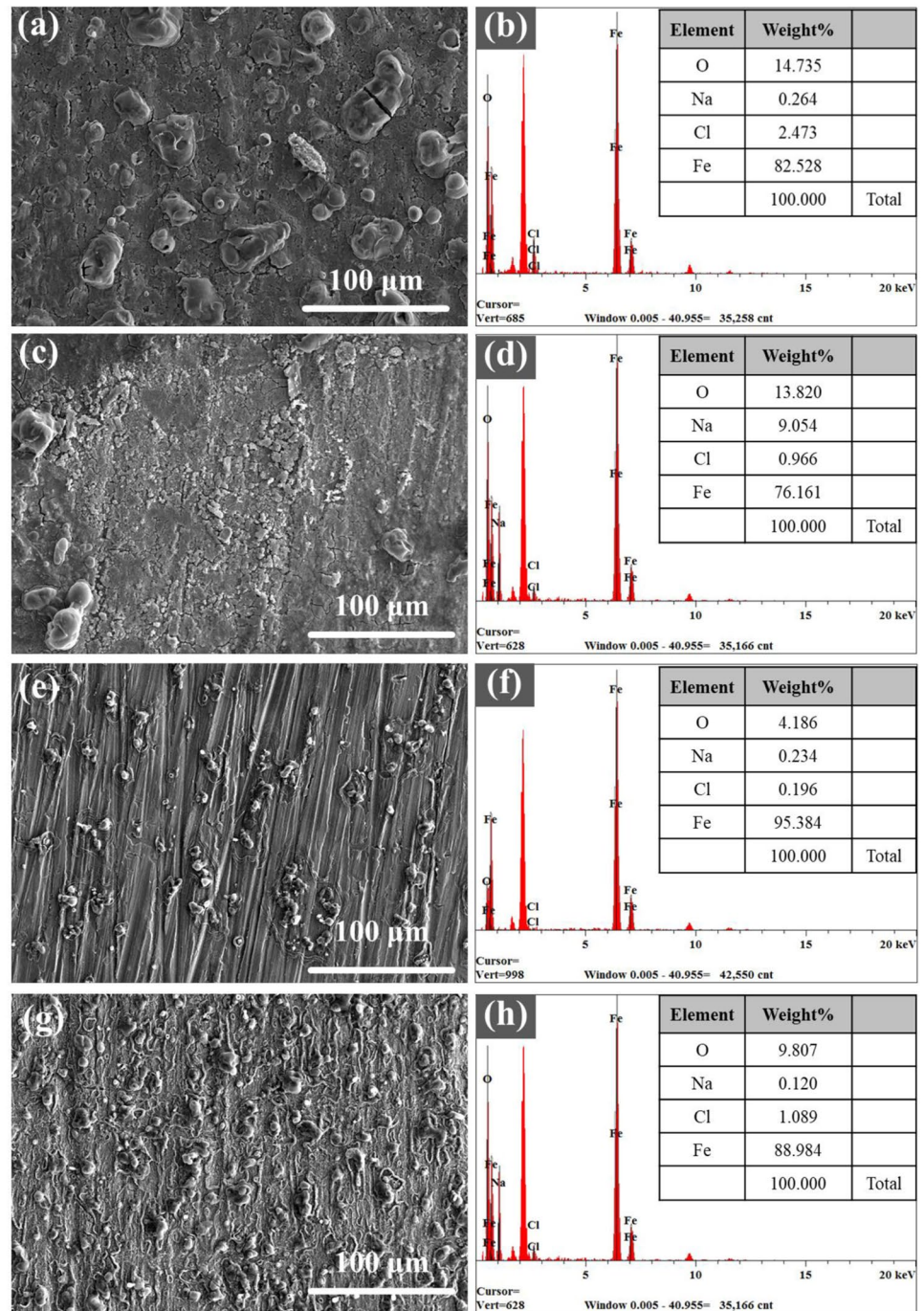


**Fig. 10** SEM images and EDS spectra of substrate coated by (a, b) blank WEP; (c, d) 0.2 wt% MXene/WEP; (e, f) 0.2 wt% fMX/WEP; and (g, h) 0.5 wt% fMX/WEP coatings after immersion in 3.5 wt% NaCl aqueous solution for 50 days

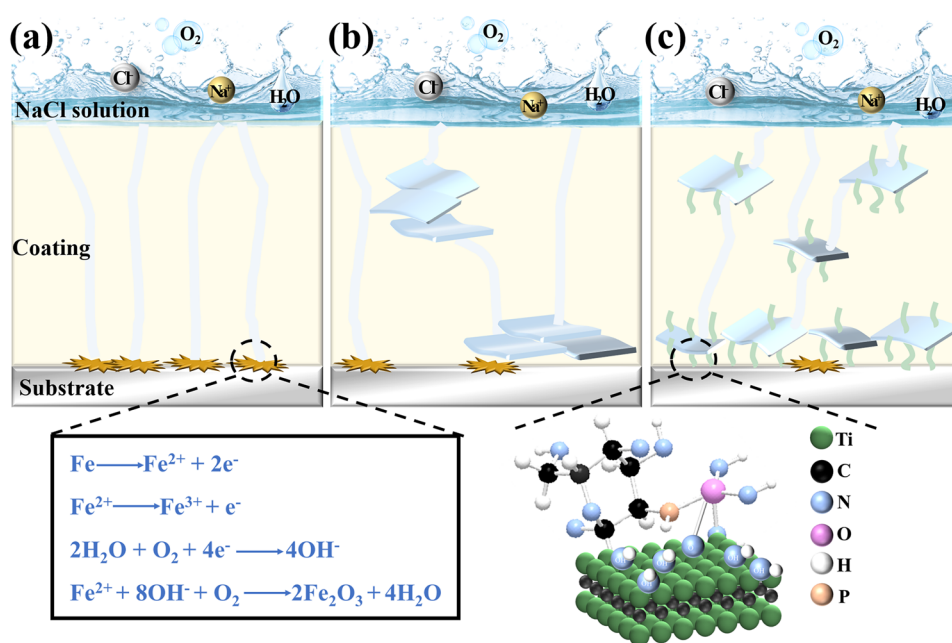


wt%) < 0.5 wt% fMX/WEP coating (9.81 wt%) < MXene/WEP coating (13.82 wt%) < blank WEP coating (14.74 wt%), as shown in Fig. 10. This means that surface of the metal protected with blank polymer has been disastrously corroded. Yet the steel plate protected with 0.2 wt% fMX/WEP coating has minimal corrosion products. Therefore, the WEP coating containing 0.2 wt% fMX shows better anti-corrosive capability than any of above coatings.

### 3.6 Anti-corrosive mechanism of nanocomposite coating

Based on the above data and analysis, it could be concluded that 0.2 wt% fMX/WEP coating exhibited the predominant anti-corrosive property. For blank WEP coating, the corrosion mediums such as water, O<sub>2</sub>, and ions can infiltrate the coatings through the micro-pores and defects, causing severe

**Fig. 11** Schematic representation of corrosion process of **a** blank WEP, **b** 0.2 wt% MXene/WEP, and **c** 0.2 wt% fMX/WEP coating



corrosion (Fig. 11). For 0.2 wt% fMX/WEP coating, the significantly enhanced anti-corrosive performance is from following aspects. On the one hand, the excellent uniform distribution of fMX nanosheets enhances the barrier ability of composite coating, prolonging the electrolyte's penetration path of corrosion medium, prolonging the electrolyte's penetration path. Furthermore, fMX has better compatibility with WEP, reducing the porosity of the coatings. On the other hand, the phosphate group in mCS has excellent metal adhesion, which reduces the degree of delamination between coating and substrate. Both factors lead to enhanced anti-corrosive performance of the coating.

## 4 Conclusions

In summary, layered MXene nanosheets, mCS, and fMX were successfully synthesized. The MXene, mCS, and fMX were investigated by FTIR, XRD, XPS, TGA, SEM, and TEM. Results of FTIR and XPS verified that mCS interacted with MXene to form Ti–O–P bond. Moreover, the *d*-spacing of MXene and fMX provided evidence for the above conclusion in the XRD patterns. Subsequently, the coatings were characterized by SEM, EDS, DSC, EIS, and PD test. The SEM and EDS of the fracture surface demonstrated that the 0.2 wt% fMX homogeneously dispersed in the coating and had brilliant compatibility with polymer matrix. Moreover, the introduction of fMX decreased the porosity of fMX/WEP coatings. After 50 days immersion in NaCl solution, the 0.2 wt% fMX/WEP coating exhibited superior anti-corrosive performance with  $|Z_{0.01\text{ Hz}}|$  of  $4.73 \times 10^7 \Omega \text{ cm}^2$ , which were two orders of magnitude higher than that of pure

coating. The  $I_{\text{corr}}$  at the 50th day was  $5.44 \times 10^{-9} \text{ A/cm}^2$ , which was two orders of magnitude lower than that of blank coating. In sum, this work will provide a novel method for designing nanocomposite coatings for high-performance and long-term metal protection.

**Supplementary information** The online version contains supplementary material available at <https://doi.org/10.1007/s42114-021-00392-0>.

**Funding** This work was supported by the National Natural Science Foundation of China (Grant Nos. 51908031 and 52003111). X. S. acknowledges the support from the Research Fund Program of Guangdong Provincial Key Lab of Green Chemical Product Technology (Grant No. GC202110). Y. C. acknowledges the support from Guangdong Special Support Program (Grant No. 2017TX04N371). J. H. acknowledges the support from the Opening Project of Key Laboratory of Polymer Processing Engineering (South China University of Technology), Ministry of Education (Grant No. KFKT2001).

## Declarations

**Conflict of interest** The authors declare no competing interests.

## References

- Huang H, Tian Y, Xie Y et al (2020) Modification of graphene oxide with acrylate phosphorus monomer via thiol-Michael addition click reaction to enhance the anti-corrosive performance of waterborne epoxy coatings. *Prog Org Coat* 146:105724. <https://doi.org/10.1016/j.porgcoat.2020.105724>
- Andreeva DV, Skorb EV, Shchukin DG (2010) Layer-by-layer polyelectrolyte/inhibitor nanostructures for metal corrosion protection. *ACS Appl Mater Interfaces* 2:1954–1962. <https://doi.org/10.1021/am1002712>

3. Lin J, Hu J, Wang W et al (2021) Thermo and light-responsive strategies of smart titanium-containing composite material surface for enhancing bacterially anti-adhesive property. *Chem Eng J* 407:125783. <https://doi.org/10.1016/j.cej.2020.125783>
4. Zhu Q, Huang Y, Li Y et al (2021) Aluminum dihydric tri-olophosphate/polypyrrole-functionalized graphene oxide waterborne epoxy composite coatings for impermeability and corrosion protection performance of metals. *Adv Compos Hybrid Mater* 4:780–792. <https://doi.org/10.1007/s42114-021-00265-6>
5. Yang X, Zhong X, Zhang J, Gu J (2021) Intrinsic high thermal conductive liquid crystal epoxy film simultaneously combining with excellent intrinsic self-healing performance. *J Mater Sci Technol* 68:209–215. <https://doi.org/10.1016/j.jmst.2020.08.027>
6. Madhusudhana AM, Mohana KNS, Hegde MB et al (2020) Functionalized graphene oxide-epoxy phenolic novolac nanocomposite: an efficient anticorrosion coating on mild steel in saline medium. *Adv Compos Hybrid Mater* 3:141–155. <https://doi.org/10.1007/s42114-020-00142-8>
7. Hu J, Lin J, Zhang Y et al (2019) A new anti-biofilm strategy of enabling arbitrary surfaces of materials and devices with robust bacterial anti-adhesion via a spraying modified microsphere method. *J Mater Chem A* 7:26039–26052. <https://doi.org/10.1039/C9TA07236E>
8. Xia Y, Zhang N, Zhou Z et al (2020) Incorporating SiO<sub>2</sub> functionalized g-C<sub>3</sub>N<sub>4</sub> sheets to enhance anticorrosion performance of waterborne epoxy. *Prog Org Coat* 147:105768. <https://doi.org/10.1016/j.porgcoat.2020.105768>
9. Yang X, Liang C, Ma T et al (2018) A review on thermally conductive polymeric composites: classification, measurement, model and equations, mechanism and fabrication methods. *Adv Compos Hybrid Mater* 1:207–230. <https://doi.org/10.1007/s42114-018-0031-8>
10. Liang C, Song P, Qiu H et al (2019) Constructing interconnected spherical hollow conductive networks in silver platelets/reduced graphene oxide foam/epoxy nanocomposites for superior electromagnetic interference shielding effectiveness. *Nanoscale* 11:22590–22598. <https://doi.org/10.1039/C9NR06022G>
11. Ma Y, Huang H, Zhou H et al (2021) Superior anti-corrosion and self-healing bi-functional polymer composite coatings with polydopamine modified mesoporous silica/graphene oxide. *J Mater Sci Technol* 95:95–104. <https://doi.org/10.1016/j.jmst.2021.04.019>
12. Yan H, Dai X, Ruan K et al (2021) Flexible thermally conductive and electrically insulating silicone rubber composite films with BNNS@Al<sub>2</sub>O<sub>3</sub> fillers. *Adv Compos Hybrid Mater* 4:36–50. <https://doi.org/10.1007/s42114-021-00208-1>
13. Song P, Liu B, Qiu H et al (2021) MXenes for polymer matrix electromagnetic interference shielding composites: a review. *Compos Commun* 24:100653. <https://doi.org/10.1016/j.coco.2021.100653>
14. Zhang Y, Ruan K, Gu J (2021) Flexible sandwich-structured electromagnetic interference shielding nanocomposite films with excellent thermal conductivities. *Small*. <https://doi.org/10.1002/sml.202101951>
15. Qi F, Wang L, Zhang Y et al (2021) Robust Ti<sub>3</sub>C<sub>2</sub>T<sub>x</sub> MXene/starch derived carbon foam composites for superior EMI shielding and thermal insulation. *Mater Today Phys*. <https://doi.org/10.1016/j.mtphys.2021.100512>
16. Yang X, Fan S, Li Y et al (2020) Synchronously improved electromagnetic interference shielding and thermal conductivity for epoxy nanocomposites by constructing 3D copper nanowires/thermally annealed graphene aerogel framework. *Compos Part Appl Sci Manuf* 128:105670. <https://doi.org/10.1016/j.compositesa.2019.105670>
17. Liang C, Qiu H, Song P et al (2020) Ultra-light MXene aerogel/wood-derived porous carbon composites with wall-like “mortar/brick” structures for electromagnetic interference shielding. *Sci Bull* 65:616–622. <https://doi.org/10.1016/j.scib.2020.02.009>
18. Yan H, Cai M, Li W et al (2020) Amino-functionalized Ti<sub>3</sub>C<sub>2</sub>T<sub>x</sub> with anti-corrosive/wear function for waterborne epoxy coating. *J Mater Sci Technol* 54:144–159. <https://doi.org/10.1016/j.jmst.2020.05.002>
19. Sun W, Wang L, Wu T et al (2015) Inhibiting the corrosion-promotion activity of graphene. *Chem Mater* 27:2367–2373. <https://doi.org/10.1021/cm5043099>
20. Cui M, Ren S, Pu J et al (2019) Poly(o-phenylenediamine) modified graphene toward the reinforcement in corrosion protection of epoxy coatings. *Corros Sci* 159:108131. <https://doi.org/10.1016/j.corsci.2019.108131>
21. Cai M, Yan H, Li Y et al (2021) Ti<sub>3</sub>C<sub>2</sub>T<sub>x</sub>/PANI composites with tunable conductivity towards anticorrosion application. *Chem Eng J* 410:128310. <https://doi.org/10.1016/j.cej.2020.128310>
22. Cui G, Guo J, Zhang Y et al (2019) Chitosan oligosaccharide derivatives as green corrosion inhibitors for P110 steel in a carbon-dioxide-saturated chloride solution. *Carbohydr Polym* 203:386–395. <https://doi.org/10.1016/j.carbpol.2018.09.038>
23. Cheng S, Chen S, Liu T et al (2007) Carboxymethylchitosan as an ecofriendly inhibitor for mild steel in 1 M HCl. *Mater Lett* 61:3276–3280. <https://doi.org/10.1016/j.matlet.2006.11.102>
24. Fayyad EM, Sadasivuni KK, Ponnamma D, Al-Maadeed MAA (2016) Oleic acid-grafted chitosan/graphene oxide composite coating for corrosion protection of carbon steel. *Carbohydr Polym* 151:871–878. <https://doi.org/10.1016/j.carbpol.2016.06.001>
25. Ruhi G, Modi OP, Dhawan SK (2015) Chitosan-polypyrrole-SiO<sub>2</sub> composite coatings with advanced anticorrosive properties. *Synth Met* 200:24–39. <https://doi.org/10.1016/j.synthmet.2014.12.019>
26. Abd El-Fattah M, El-Saeed AM, Azzam AM et al (2016) Improvement of corrosion resistance, antimicrobial activity, mechanical and chemical properties of epoxy coating by loading chitosan as a natural renewable resource. *Prog Org Coat* 101:288–296. <https://doi.org/10.1016/j.porgcoat.2016.09.002>
27. Jayakumar R, Nagahama H, Furuie T, Tamura H (2008) Synthesis of phosphorylated chitosan by novel method and its characterization. *Int J Biol Macromol* 42:335–339. <https://doi.org/10.1016/j.ijbiomac.2007.12.011>
28. Yu H, Xu X, Xia Y et al (2020) Synthesis of a novel modified chitosan as an intumescent flame retardant for epoxy resin. *E-Polym* 20:303–316. <https://doi.org/10.1515/epoly-2020-0036>
29. Zheng B, Mao C, Gu T et al (2019) Phosphorylated chitosan to promote biomimetic mineralization of type I collagen as a strategy for dentin repair and bone tissue engineering. *New J Chem* 43:2002–2010. <https://doi.org/10.1039/C8NJ04889D>
30. Lu X, Huang H, Zhang X et al (2019) Novel light-driven and electro-driven polyethylene glycol/two-dimensional MXene form-stable phase change material with enhanced thermal conductivity and electrical conductivity for thermal energy storage. *Compos Part B Eng* 177:107372. <https://doi.org/10.1016/j.compositesb.2019.107372>
31. Zhou Y, Lin Y, Tawiah B et al (2021) DOPO-decorated two-dimensional MXene nanosheets for flame-retardant, ultraviolet-protective, and reinforced polylactide composites. *ACS Appl Mater Interfaces* 13:21876–21887. <https://doi.org/10.1021/acsami.1c05587>
32. Wei Y, Luo W, Zhuang Z et al (2021) Fabrication of ternary MXene/MnO<sub>2</sub>/polyaniline nanostructure with good electrochemical performances. *Adv Compos Hybrid Mater*. <https://doi.org/10.1007/s42114-021-00323-z>
33. Sheng X, Zhao Y, Zhang L, Lu X (2019) Properties of two-dimensional Ti<sub>3</sub>C<sub>2</sub> MXene/thermoplastic polyurethane nanocomposites with effective reinforcement via melt blending. *Compos Sci Technol* 181:107710. <https://doi.org/10.1016/j.compscitech.2019.107710>
34. Osti NC, Naguib M, Ostadhossein A et al (2016) Effect of metal ion intercalation on the structure of MXene and water dynamics

- on its internal surfaces. *ACS Appl Mater Interfaces* 8:8859–8863. <https://doi.org/10.1021/acsami.6b01490>
35. Yazdanparast S, Soltanmohammad S, Fash-White A et al (2020) Synthesis and surface chemistry of 2D TiVC solid-solution MXenes. *ACS Appl Mater Interfaces* 12:20129–20137. <https://doi.org/10.1021/acsami.0c03181>
  36. Ungár T (2004) Microstructural parameters from X-ray diffraction peak broadening. *Scr Mater* 51:777–781. <https://doi.org/10.1016/j.scriptamat.2004.05.007>
  37. Amaral IF, Granja PL, Barbosa MA (2005) Chemical modification of chitosan by phosphorylation: an XPS, FT-IR and SEM study. *J Biomater Sci Polym Ed* 16:1575–1593. <https://doi.org/10.1163/156856205774576736>
  38. Wang Y, Liu Z, Wei X et al (2021) An integrated strategy for achieving oil-in-water separation, removal, and anti-oil/dye/bacteria-fouling. *Chem Eng J* 413:127493. <https://doi.org/10.1016/j.cej.2020.127493>
  39. Chen C-H, Wang F-Y, Mao C-F et al (2008) Studies of chitosan: II. Preparation and characterization of chitosan/poly(vinyl alcohol)/gelatin ternary blend films. *Int J Biol Macromol* 43:37–42. <https://doi.org/10.1016/j.ijbiomac.2007.09.005>
  40. Halim J, Cook KM, Naguib M et al (2016) X-ray photoelectron spectroscopy of select multi-layered transition metal carbides (MXenes). *Appl Surf Sci* 362:406–417. <https://doi.org/10.1016/j.apsusc.2015.11.089>
  41. Raj KJA, Shanmugam R, Mahalakshmi R, Viswanathan B (2010) XPS and IR spectral studies on the structure of phosphate and sulphate modified titania – a combined DFT and experimental study. *IJC- Vol49A01 January 2010*
  42. Gao Q, Pan Y, Zheng G et al (2021) Flexible multilayered MXene/thermoplastic polyurethane films with excellent electromagnetic interference shielding, thermal conductivity, and management performances. *Adv Compos Hybrid Mater* 4:274–285. <https://doi.org/10.1007/s42114-021-00221-4>
  43. Liu X, Guo J, Tang W et al (2019) Enhancing the flame retardancy of thermoplastic polyurethane by introducing montmorillonite nanosheets modified with phosphorylated chitosan. *Compos Part Appl Sci Manuf* 119:291–298. <https://doi.org/10.1016/j.compositesa.2019.02.009>
  44. Maleski K, Mochalin VN, Gogotsi Y (2017) Dispersions of two-dimensional titanium carbide MXene in organic solvents. *Chem Mater* 29:1632–1640. <https://doi.org/10.1021/acs.chemmater.6b04830>
  45. Zhou X, Huang H, Zhu R et al (2019) Facile modification of graphene oxide with lysine for improving anti-corrosion performances of water-borne epoxy coatings. *Prog Org Coat* 136:105200. <https://doi.org/10.1016/j.porgcoat.2019.06.046>
  46. Tikhani F, Jouyandeh M, Jafari SH et al (2019) Cure index demonstrates curing of epoxy composites containing silica nanoparticles of variable morphology and porosity. *Prog Org Coat* 135:176–184. <https://doi.org/10.1016/j.porgcoat.2019.05.017>
  47. Zhang L, Li CZ, Zhou Q, Shao W (2007) Aluminum hydroxide filled ethylene vinyl acetate (EVA) composites: effect of the interfacial compatibilizer and the particle size. *J Mater Sci* 42:4227–4232. <https://doi.org/10.1007/s10853-006-0630-6>
  48. Sheng X, Mo R, Ma Y et al (2019) Waterborne epoxy resin/polydopamine modified zirconium phosphate nanocomposite for anti-corrosive coating. *Ind Eng Chem Res* 58:16571–16580. <https://doi.org/10.1021/acs.iecr.9b02557>
  49. Zheng S, Bellido-Aguilar DA, Hu J et al (2019) Waterborne bio-based epoxy coatings for the corrosion protection of metallic substrates. *Prog Org Coat* 136:105265. <https://doi.org/10.1016/j.porgcoat.2019.105265>
  50. Bonora PL, Deflorian F, Fedrizzi L (1996) Electrochemical impedance spectroscopy as a tool for investigating underpaint corrosion. *Electrochim Acta* 41:1073–1082. [https://doi.org/10.1016/0013-4686\(95\)00440-8](https://doi.org/10.1016/0013-4686(95)00440-8)
  51. Mahdavian M, Attar MM (2009) Electrochemical behaviour of some transition metal acetylacetonate complexes as corrosion inhibitors for mild steel. *Corros Sci* 51:409–414. <https://doi.org/10.1016/j.corsci.2008.11.010>
  52. Hamdy AS, Doench I, Möhwald H (2011) Smart self-healing anti-corrosion vanadia coating for magnesium alloys. *Prog Org Coat* 72:387–393. <https://doi.org/10.1016/j.porgcoat.2011.05.011>
  53. Li Z, Qin B, Zhang X et al (2015) Self-healing anti-corrosion coatings based on polymers of intrinsic microporosity for the protection of aluminum alloy. *RSC Adv* 5:104451–104457. <https://doi.org/10.1039/C5RA19614K>
  54. Wang N, Zhang Y, Chen J et al (2017) Dopamine modified metal-organic frameworks on anti-corrosion properties of waterborne epoxy coatings. *Prog Org Coat* 109:126–134. <https://doi.org/10.1016/j.porgcoat.2017.04.024>
  55. Huang H, Li M, Tian Y et al (2020) Exfoliation and functionalization of  $\alpha$ -zirconium phosphate in one pot for waterborne epoxy coatings with enhanced anticorrosion performance. *Prog Org Coat* 138:105390. <https://doi.org/10.1016/j.porgcoat.2019.105390>
  56. Coquery C, Negrell C, Caussé N et al (2019) Synthesis of new high molecular weight phosphorylated chitosans for improving corrosion protection. *Pure Appl Chem* 91:509–521. <https://doi.org/10.1515/pac-2018-0509>
  57. Soleymanibrojeni M, Shi H, Udoh II et al (2019) Microcontainers with 3-amino-1,2,4-triazole-5-thiol for enhancing anticorrosion waterborne coatings for AA2024-T3. *Prog Org Coat* 137:105336. <https://doi.org/10.1016/j.porgcoat.2019.105336>
  58. Hayatgheib Y, Ramezanzadeh B, Kardar P, Mahdavian M (2018) A comparative study on fabrication of a highly effective corrosion protective system based on graphene oxide-polyaniline nanofibers/epoxy composite. *Corros Sci* 133:358–373. <https://doi.org/10.1016/j.corsci.2018.01.046>
  59. Cui M, Ren S, Qin S et al (2018) Processable poly(2-butylaniline)/hexagonal boron nitride nanohybrids for synergetic anticorrosive reinforcement of epoxy coating. *Corros Sci* 131:187–198. <https://doi.org/10.1016/j.corsci.2017.11.022>

**Publisher's Note** Springer Nature remains neutral with regard to jurisdictional claims in published maps and institutional affiliations.